Journal of ELECTRONIC MATERIALS, Vol. 44, No. 10, 2015
DOI: 10.1007/s11664-015-3790-9

Molybdenum Oxides Deposited by Modulated Pulse Power Magnetron Sputtering: Stoichiometry as a Function of Process Parameters

NEIL R. MURPHY,[1,4] LIRONG SUN,[1,2,5] JOHN T. GRANT,[1,3,6] JOHN G. JONES,[1,7] and RACHEL JAKUBIAK[1,8]

1.—Air Force Research Laboratory, Materials and Manufacturing Directorate, Wright-Patterson Air Force Base (WPAFB), 2977 Hobson Way, Dayton, OH 45433, USA. 2.—General Dynamics Information Technology, 5100 Springfield Street, Dayton, OH 45431, USA. 3.—Research Institute, University of Dayton, 300 College Park, Dayton, OH 45469, USA. 4.—e-mail: neil.murphy.1@us.af.mil. 5.—e-mail: lirong.sun.2.ctr@us.af.mil. 6.—e-mail: john.grant.5.ctr@us.af.mil. 7.—e-mail: John.jones.66@us.af.mil. 8.—e-mail: rachel.jakubiak@us.af.mil

Molybdenum oxide films were deposited using modulated pulse power magnetron sputtering (MPPMS) from a molybdenum target in a reactive environment where the flow rate of oxygen was varied from 0 sccm to 2.00 sccm. By varying the amount of reactive oxygen available during deposition, the composition of the films ranged from metallic Mo to fully stoichiometric MoO_3, when the molybdenum target became poisoned, due to the formation of a dielectric surface oxide coating. Film compositions were verified using high energy resolution x-ray photoelectron spectroscopy. Target poisoning occurred at an oxygen flow rate of 1.25 sccm and reversed when the flow rate decreased to about 1.00 sccm. MoO_3 films deposited via MPPMS had densities of 3.8 g cm^{-3}, 81% of the density of crystalline α-MoO_3 as determined by x-ray reflectivity (XRR). In addition, XRR and atomic force microscopy data showed sub-nanometer surface roughness values. From spectroscopic ellipsometry, the measured refractive index of the MoO_3 films at 589 nm was 1.97 with extinction coefficient values <0.02 at wavelengths above the measured absorption edge of 506 nm (2.45 eV).

Key words: Molybdenum oxide, reactive magnetron sputtering, MPPMS, XPS, MoO_3

INTRODUCTION

Molybdenum Oxide

Molybdenum oxide thin films find use in many technological areas including catalysis,[1–5] optics,[6,7] electronics,[5,8–15] and chemical sensing,[5,9,16–18] to name a few. The diversity of these applications can be attributed to the wide range of oxidation states (0–VI) accommodated by molybdenum[2,5,19] and the facile manipulation of those states via oxidation or reduction. In its fully oxidized state (VI), molybdenum trioxide (MoO_3) is optically transparent with a band gap that ranges from 2.67 eV to 3.12 eV.[5,9,20] MoO_3 also exhibits dynamic coloration via reduction induced by UV irradiation (photochromism),[5,9] charge injection (electrochromism),[9,21] or heat treatment (thermocoloration).[22] Additional oxide compounds formed by molybdenum include the "surface phase" Mo_2O_5 (Mo(V)), which has no known bulk structure,[23–25] and MoO_2 (Mo(IV)), commonly present in the distorted rutile structure.[26] While not as widely investigated as MoO_3, MoO_2 is electrically conductive and has shown significant promise for use as an anode material within lithium ion batteries.[27–31]

As a result of the breadth of their technological applications, several physical vapor deposition methods for fabricating molybdenum oxide thin films have been explored. Such methods include, but

(Received May 28, 2014; accepted April 9, 2015; published online May 27, 2015)

are not limited to, spray pyrolysis,[32–34] thermal evaporation,[21,35,36] pulsed laser deposition,[37–39] radio frequency magnetron sputtering,[40,41] and reactive DC magnetron sputtering.[9,20,37,42,43] While all of the aforementioned techniques are capable of depositing high quality films when performed under optimal conditions, studies employing reactive DC magnetron sputtering have generated significant interest due to the industrial scalability of magnetron sputtering techniques, as well as the high degree of control over the oxidation state as a function of reactive oxygen availability.[9,20,37,42,43] Previous works of note include studies performed by Mohamed et al. demonstrating a comprehensive correlation between oxygen partial pressure and the resulting crystallinity, chemistry, and optical behavior of molybdenum oxide thin films.[9] While numerous studies have confirmed that it is possible to obtain high-quality molybdenum oxide thin films via DC magnetron sputtering, the advent of a technique known as modulated pulse power magnetron sputtering (MPPMS) has shown promise for further optimization. Specifically, the high target power densities, ($\sim$500 W/cm^2) associated with MPPMS are capable of achieving a highly metallic deposition flux.[44–46] Reports by Hala et al. have indicated that the high power densities and variable pulse profiles associated with the MPPMS process are directly correlated to the reduction in process instability associated with the formation of a dielectric, or "poisoned" surface oxide layer, on the sputter target.[46] In addition, ion bombardment associated with MPPMS has been reported to improve film adhesion, while reducing surface roughness and providing increases in density.[44,46,47] Finally, a high degree of control over the magnitude and duration of MPPMS discharge events has been reported to reduce arcing, limit hysteresis when sputtering in reactive regimes, and tailor ionization levels of inert, reactive and metallic components in the plasma.[44,46,48–52] The ability to leverage ionization levels of both reactive and metallic components could be of considerable benefit for controlling the chemistry and structure of molybdenum oxide thin films.

This study was performed in order to analyze the effect of systematic changes in the oxygen flow rate on the structural, chemical, and optical properties of thin (<60 nm) molybdenum oxide films deposited using MPPMS. Of particular interest is the potential application of MoO_3 (Mo(VI)) in optical interference coatings where smooth, amorphous, thin, transparent, variable index materials are desirable. To our knowledge, there are currently no reports on the deposition and characterization of MPPMS-deposited oxides of molybdenum.

MATERIALS AND METHODS

Experimental Conditions

Molybdenum oxide films were deposited within a stainless steel high-vacuum chamber equipped with multiple magnetron sputtering sources. Prior to deposition, the chamber was evacuated to a base pressure of at least 4.0×10^{-5} Pa (3.0×10^{-7} Torr). All magnetron guns were retracted and films were deposited using a single 50-mm source placed 9 cm from the surface of the substrate. A working pressure of 1.33 Pa (10 mTorr) was maintained throughout all depositions. Due to the variations in pressure associated with the use of reactive gasses,[53–56] pumping speed was varied using an automated conductance controller. The source material was a 99.99% pure molybdenum target (K.J. Lesker) magnetically attached to a 50-mm-diameter, unbalanced magnetron source (MeiVac). Films were deposited on prime grade 50-mm-diameter (001) *p*-type silicon wafers (University Wafer) and also on 25-mm-diameter quartz discs (Machine Glass Specialists) for the optical transmission measurements, with no bias or external heating applied to the substrates. The substrates rotated at 7.7 rpm to reduce anisotropy imparted by the sputtering process.

Research grade argon (99.999%; Airgas) and oxygen (99.999%; Wieler Welding) facilitated the reactive sputtering process. The oxygen flow rate ($f_{(O_2)}$) and argon flow rate ($f_{(Ar)}$) were controlled using MKS mass flow controllers with a maximum flow rate of 20.00 $\pm$ 0.04 sccm. The MPPMS process used a Zpulser AXIA™ magnetron discharge generator operated in manual mode with the capacitors charged to 300 V and a macropulse frequency of 50 Hz. MPPMS is a derivative of the high-power impulse magnetron sputtering (HIPIMS) technique introduced by Kouznetsov et al. in 1999.[57] Both techniques utilize high target power densities at duty cycles <10%.[49,50,57,58] Key differences between the two techniques involve the shape, duration and magnitudes of the voltage pulses applied to the cathode. HIPIMS, consisting of square voltage pulses lasting <200 μs, achieves target power densities of the order of 1–3 kW/cm^2.[45–47,58] MPPMS, on the other hand, is slightly less aggressive, utilizing longer overall pulses (>1 ms) at power densities approaching 500 W/cm^2.[44–46] Unlike HIPIMS, the voltage pulses applied in the MPPMS technique consist of multiple microsecond-length pulses, known as "micropulses", rather than just one square pulse. Micropulses typically last between 1 μs and 15 μs and can be varied with high precision to allow for the user to specify their frequency. The frequency of the microscale pulse application is directly related to the magnitude of the longer (>1 ms) macroscale voltage pulse.[47–49] A two-part pulse was created similar to that specified by Hála et al.[46] The first stage of the pulse generated a low energy plasma discharge with a duration of 400 μs derived from a 20% micropulse duty cycle, and the second stage consists of a higher energy plasma lasting 600 μs controlled by micropulses applied at a 54.5% duty cycle with an on time of 12 μs and an off time of 10 μs as illustrated in Fig. 1. The total

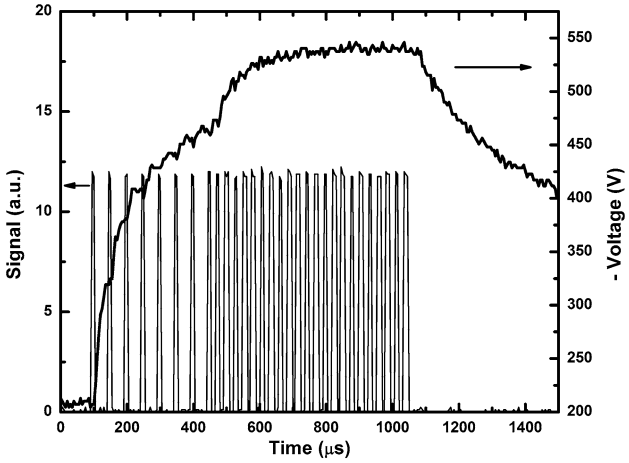

Fig. 1. Pulse generation via MPPMS. The thin line represents voltage signal on and off time generated by the power supply, the bold line is the resulting cathode voltage.

macroscale duty cycle for the MPPMS deposition process was 5%. During depositions, the MPPMS power supply was operated in constant voltage mode and normalized to obtain an average power of 80 W at $f_{(O_2)}$ = 0 sccm. Changes in voltage and current output were analyzed using a Tektronix® DPO 5204 multi-channel oscilloscope.

Time-averaged optical emission spectroscopy (OES) allowed qualitative analysis of the relative concentrations of Ar and Mo species in the plasma discharge. Optical emission generated during the deposition process was collected by an external fiber optic placed directly before a quartz viewport 45 cm from the plume. Spectra were processed with an OceanOptics USB 4000 spectrometer using an integration time of 500 ms and dark correction to reduce the effects of ambient light prior to plasma ignition.

Chemical, Optical and Structural Characterization

Characterization of the structure of these films used multiple analysis methods. Surface roughness was quantified using a Veeco Instruments atomic force microscope (AFM) with a NanoScope® V controller. Five scan regions were selected and scanned in tapping mode with a scan area of 25 μm^2. To determine the film thickness and optical dispersion, *in situ* spectroscopic ellipsometry (SE) data were collected throughout the deposition process using a J.A. Woollam M-2000® VI ellipsometer that operated in the 371–1678 nm wavelength range. Surface roughness (AFM) and thickness (ellipsometry) measurements were verified with x-ray reflectivity (XRR) (Rigaku SmartLab®). Crystallinity was measured with grazing incidence x-ray diffraction (GIXRD) (Rigaku SmartLab®) using an incidence angle of 0.35°, a resolution of 0.01°, and a detector angle of 2θ. The x-ray source, Cu Kα (1.5418 Å), was operated at 40 kV and 44 mA. Optical transmission and reflectivity data were measured with a Perkin-Elmer ® Lambda 1050 UV/Vis/NIR spectrophotometer with an integrating sphere attachment. Transmission and reflectivity values were used in the calculation of the optical bandgap, E_g.

Surface analysis via x-ray photoelectron spectroscopy (XPS) was employed in order to analyze the composition and chemistry of the films. All scans were collected using a Physical Electronics 5700 XPS with a monochromatic aluminum x-ray source at a photon energy of 1486.7 eV. Survey scans were taken at an analyzer pass energy of 187.85 eV, while high resolution scans used a pass energy of 29.35 eV. Survey scans were taken for binding energies from 0 eV to 1400 eV, while high energy resolution scans capturing the molybdenum 3d doublet, were acquired from 220 eV to 245 eV. For convenience, all spectra were energy calibrated with respect to the adventitious carbon 1 s transition at a binding energy of 284.6 eV. Fitting of the XPS spectra employed the CasaXPS 2.3.16 software package.[59] Parameters including full width at half-maximum peak height, location of peak center and peak area were determined after using a Shirley background subtraction. A mixed Gaussian–Lorentzian line shape was used for the peak fitting.

RESULTS AND DISCUSSION

Reactive Magnetron Sputtering of Molybdenum Oxide

As the oxygen flow rates varied, the changes in the voltage and current evolved from the plasma discharge were monitored. An average power of 80 W with $f_{(Ar)}$ = 20 sccm and $f_{(O_2)}$ = 0 operating at 1.33 Pa (10 mTorr) yielded an average power of 1600 W per pulse. The average power per pulse is calculated by dividing the total average power of 80 W by the 5% duty cycle. The oxygen flow rates used for deposition were selected by measuring the onset of target poisoning, wherein the entire target surface is coated with molybdenum–oxygen compounds. The transition from a metallic target surface to an oxidized target surface is accompanied by a precipitous drop in both current and deposition rate.[53,54,60] Power levels were plotted as a function of oxygen flow rate, which was increased from 0.00 sccm to 2.00 sccm, at intervals of 0.25 sccm (Fig. 2). The total flow rate ranged between 20 sccm and 22 sccm depending on the amount of oxygen added to the chamber. In order to maintain a working pressure of 1.33 Pa (10 mTorr) under different flow rates, the pumping speed varied between 50 L/s and 60 L/s. Pumping speeds were calculated using the method outlined by Dushman.[61] A dwell period of 90 s was used at each flow rate prior to recording the voltage and current. Upon fully poisoning the target at $f_{(O_2)}$ = 2.00 and $f_{(Ar)}$ = 20.00 sccm, $f_{(O_2)}$ was then reduced to zero at increments of 0.25 sccm. Reduction of $f_{(O_2)}$ was performed in order to analyze the change in oxygen content required to remove the

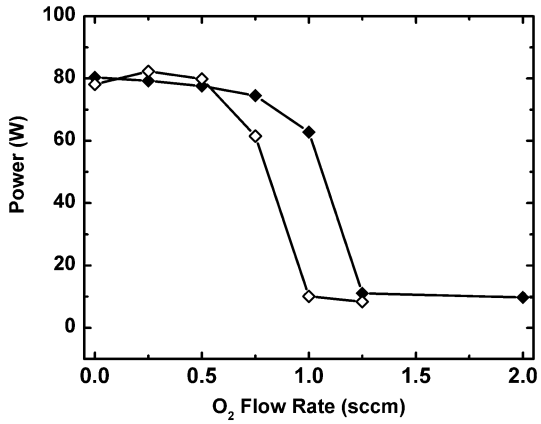

Fig. 2. Power output as a function of increasing (solid circles) and decreasing (open circles) oxygen flow rates for MPPMS.

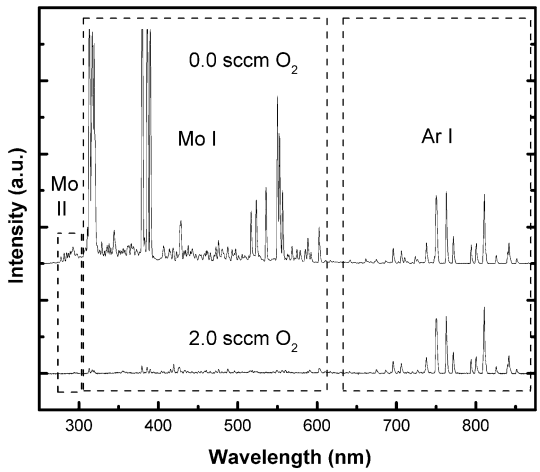

Fig. 3. Optical emission spectra obtained for MPPMS plasmas. Data were collected during MoO_x depositions using oxygen flow rates of 0.00 sccm (top) and 2.00 sccm (bottom) and 20 sccm Ar for both. The saturation in the upper spectrum is a result of the collection time (500 ms) used to accommodate optical emission intensity.

oxide layer from the target. As Fig. 2 illustrates, a measureable degree of hysteresis exists between the flow rates required to poison the target and those necessary to recover the metallic target surface. At $f_{(O_2)} \leq 0.75$ sccm, the plasma flux acts as a getter, reacting with all of the oxygen within the chamber; however, once $f_{(O_2)}$ exceeds 0.75 sccm, the excess oxygen that is not reacting within the deposition flux begins to adsorb onto the chamber surfaces, including the surface of the target.

Compound formation on the target surface, in this case oxidation, leads to a reduction in the net power achieved by the plasma discharge. At values of $f_{(O_2)} \geq 1.25$ sccm the power evolved is no longer affected by the changing oxygen flow, indicating that the target surface has fully reacted. As shown in Fig. 2, it is evident that the initial drop in power occurs at $f_{(O_2)} = 0.75$ sccm. Figure 2 demonstrates that the power output for the MPPMS technique drops precipitously at a $f_{(O_2)} = 1.00$ sccm. The rapid loss of power, coinciding with decreased current, is a result of several factors. First, the introduction of oxygen within the chamber reduces the number of free electrons within the plasma as a result of the formation of oxygen ions.[38] Additional losses in current are likely brought on by the inhibition of ion-induced secondary electron emission (ISEE) associated with compound formation on the target surface.[46,49,52,56,62,63] While documentation of the Ar^+-induced emission of secondary electrons for oxidized molybdenum is limited, studies by Depla et al. on the ISEE of Nb, Ta, and Re, have indicated significant reductions in secondary electron emission as a result of surface oxidation.[56] Reduction of the number of secondary electrons emitted leads to a net decrease in electron density near the surface of the cathode, resulting in the occurrence of fewer ionization events responsible for sputtering.[53,54,56,64,65] Thus, surface oxidation appears to be the main factor in the decrease in current, and, subsequently, deposition rate. The ISEE is a function of the ion energy, therefore it will be dependent upon the voltage applied to the cathode.[46,56,62] Note that instantaneous cathode voltage levels for films deposited at $0 \leq f_{(O_2)} \leq 2$ sccm range from 550 volts to 610 volts.

Optical Emission Spectroscopy

Additional analysis of the effect of oxygen flow on power output and plasma discharge was conducted using OES. Figure 3 contains the optical emission spectra of Ar and Mo when $f_{(O_2)} = 0.0$ sccm and $f_{(Ar)} = 20$ sccm as well as the spectra at $f_{(O_2)} = 2.0$ sccm and $f_{(Ar)} = 20$ sccm. Under these conditions, the relative concentrations of both excited argon (Ar I, 650–875 nm) and molybdenum peaks (Mo I, 300–610 nm) of the plasmas differ significantly. As a result of the high power density experienced by the target during MPPMS, the plasma appears highly metallic in character, with a relatively small contribution from Ar-related optical emission. Further, the high target power density associated with MPPMS has the potential to cause target atom ionization,[5,44,47,48,66] as evinced by peaks shorter than 280 nm attributed to singly ionized molybdenum (Mo II).[35] These same peaks are not readily detectable in the optical emission attributed to the poisoned Mo target at $f_{(O_2)} = 2.0$ sccm. In the poisoned regime ($f_{(O_2)} \geq 1.25$ sccm) the magnitude of the optical emission signal from Mo is greatly reduced. As expected, target oxidation and subsequent current reduction drastically reduces molybdenum photoemission within the plasma.

X-ray Photoelectron Spectroscopy

XPS analysis was used to determine the composition and chemistry of MPPMS deposited samples that were fabricated at $f_{(O_2)} = 0.00$ sccm, 0.75 sccm, 1.00 sccm, 1.25 sccm, and 2.00 sccm. For each specimen, a survey spectrum (Fig. 4) and high resolution

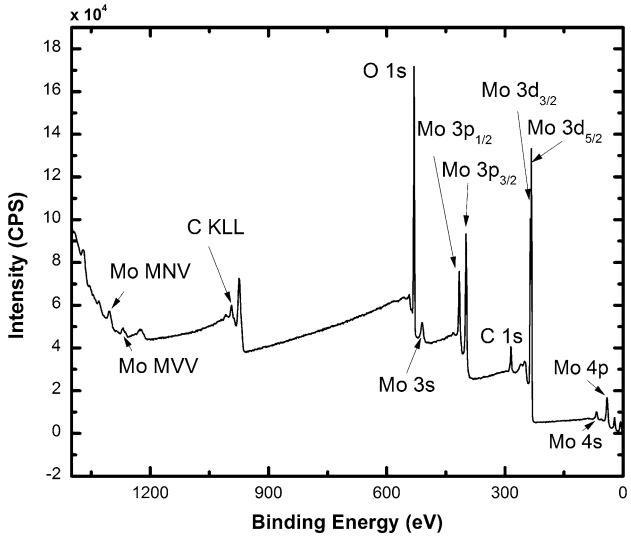

Fig. 4. Survey spectrum of fully stoichiometric MoO_3 deposited at an oxygen flow rate of 2.00 sccm O_2 and 20.00 sccm Ar at 1.33 Pa (10 mTorr).

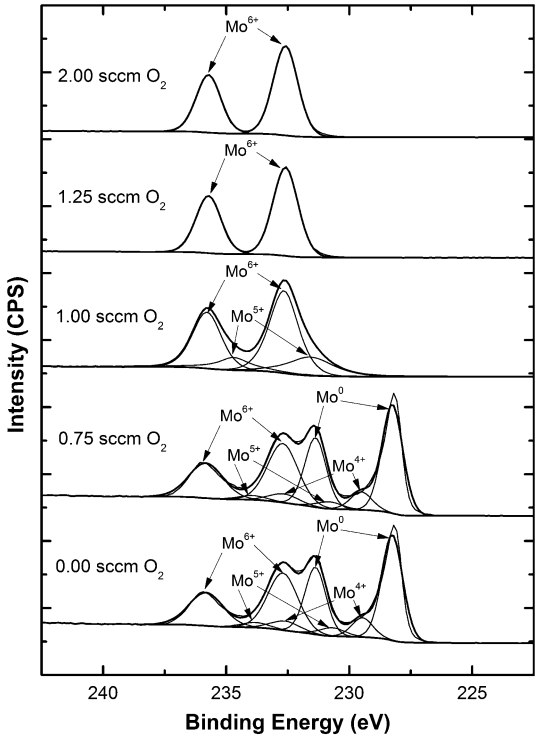

Fig. 5. High resolution XPS spectra of the Mo 3d transitions for depositions at flow rates of 0.00 sccm, 0.75 sccm, 1.00 sccm, 1.25 sccm, and 2.00 sccm O_2. Spectra are offset for clarity and peak assignments are given.

spectrum (Fig. 5) were obtained. Chemical analysis using XPS indicated that the oxidation state and associated stoichiometry of the as-grown films was highly sensitive to the oxygen flow rate. Survey scans of representative films ($f_{(O_2)}$ = 0.00 sccm to 2.00 sccm) were acquired in order to quantify the presence of various elements within the films. Peak shapes and binding energies (Mo 3d) of high resolution scans were used to determine stoichiometry. All films analyzed via XPS were exposed to atmosphere prior to measurement since the growth and analysis chambers were separate. As a consequence of environmental exposure, all the films analyzed contain 23–30 at.% of adventitious carbon on their respective surfaces. Note that spectra were calibrated with respect to the carbon 1 s transition with a binding energy of 284.6 eV.

High energy resolution XPS yielded detailed information regarding the oxidation state of the molybdenum. The presence of oxidation state Mo^{6+} was indicative of the compound MoO_3, while the presence of Mo^{5+} and Mo^{4+} was associated with substoichiometric compounds including Mo_2O_5 and MoO_2 (Table I).[2,20,21,43,67,68–71] Furthermore, at $f_{(O_2)} < 1.00$ sccm, metallic Mo was also present. It is highly likely that small quantities of additional suboxides were present within the films; however, their presence was indistinguishable from the uncertainty inherent in the peak fitting process. In the case of multiple doublets resulting from the presence of different oxidation states, the doublet spacing (3.13 eV)[70] and peak area ratios were kept constant during peak fitting. The area of the $3d_{5/2}$ peak was constrained to be 1.5 times that of the peak associated with the $3d_{3/2}$ transition.[70,72] In order to account for the asymmetry inherent in the 3d transition for metallic Mo, 3d transitions from an experimentally obtained Mo reference were measured and subsequently used to perform fits. Films deposited at $f_{(O_2)}$ = 0.00 sccm and 0.75 sccm were found to be mostly metallic in character, and the presence of the Mo^{5+} and Mo^{4+} oxidation states was the result of environmental exposure, as subsequent analysis after 1 min of ion beam sputtering produced spectra consistent with that of metallic molybdenum. Interrogation of the valence state as a function of $f_{(O_2)}$ demonstrates the flexibility of the MPPMS process, indicating the ability to selectively control the presence of Mo_2O_5 (Mo(V)) within an MoO_3 (Mo(VI)) matrix. However, with regard to the various oxides of molybdenum, pure MoO_3 is the preferred chemical constituent within optical coatings due to its transparent, dielectric behavior. While Mo_2O_5 (Mo(V)) and MoO_2 (Mo(IV)) have very interesting electronic properties, the onset of the deposition of transparent MoO_3 is of particular interest within this study. According to data obtained from high resolution spectra, molybdenum trioxide films were only obtainable at oxygen partial pressures at or above the threshold for target poisoning, corresponding to $f_{(O_2)}$ = 1.25 sccm.

Spectroscopic Ellipsometry

Analysis of data collected from *in situ* SE provided values for the thickness and the real (n) and imaginary (k) components of the refractive index. To

Table I. Experimentally determined binding energies (eV) for various oxidation states of molybdenum

Compound	Valence state	Measured binding energy (eV)		Reference values (eV)		Reference
		$3d_{3/2}$	$3d_{5/2}$	$3d_{3/2}$	$3d_{5/2}$	
MoO_3	VI	235.72	232.59	235.70	232.51	27
Mo_2O_5	V	234.69	231.56	234.36	231.17	27
MoO_2	IV	232.64	229.51	231.8	228.7	65
Mo	0	231.38	228.25	231.13	228.00	65

obtain these values, the raw amplitude (ψ) and phase difference (Δ) data collected by the ellipsometer were fit with a general oscillator model containing a Cauchy layer; a model commonly used for high energy bandgap materials such as molybdenum trioxide, due to the minimal absorption ($k \approx 0$) as well as exponential decay of the refractive index (n) as a function of decreasing photon energy.[72] The optical constants of films deposited in the poisoned regime ($f_{(O_2)} > 1.00$ sccm) were modeled using a general oscillator model with two Tauc-Lorentz oscillators to account for the free-carrier absorption associated with substoichiometric molybdenum oxide compounds, Mo_2O_5, MoO_2, and metallic Mo and their respective oxidation states, V, IV, and 0. Film thicknesses were also determined as well as the deposition rates. Those values are given in Table II.

Metallic-rich films deposited at $f_{(O_2)} < 1.25$ exhibit characteristically higher n and k values than fully oxidized samples deposited in the poisoned regime ($f_{(O_2)} > 1.00$), similar to that described by He and Yao.[5] As shown in Fig. 6a, in the visible to near IR spectral range (371–1678 nm), the index (n) of the metallic samples spans from a minimum of 2.1 at 381 nm to 3.7 at 760 nm. At wavelengths >1200 nm, the index fluctuates slightly around a value of $n = 2.5$. The MoO_3 films prepared in the poisoned target regime have the same index as the metallic films at $\lambda = 371$ nm; however, the index gradually decreases to a constant value of 1.86 starting at 800 nm and remains nearly invariant out through 1678 nm. Additionally, those films have negligible extinction coefficients ($k < 1 \times 10^{-3}$) at energies below the onset of the absorption edge located at 506 nm (Fig. 6b). In contrast, the k of films fabricated in the non-poisoned regime, increase monotonically from 3.1 to 7.5 with wavelength. Films deposited in the transition region between the metallic and poisoned regime ($f_{(O_2)} < 1.25$ sccm), exhibit optical dispersion that falls between that of the MoO_3 and metallic films.

A plot of the refractive index and extinction coefficients as a function of $f_{(O_2)}$ at wavelengths of 632 nm, 900 nm and 1200 nm (Fig. 7) illustrates the effect of oxygen flow rate on the optical properties of the films. As the partial pressure of oxygen increases, the optical constants begin to change as a result of the transition between metallic and dielectric character. XPS measurements, as

Table II. Thickness (d) and deposition rate (σ) for molybdenum oxide films deposited at varying oxygen flow rates ($f_{(O_2)}$)

$f_{(O_2)}$ (sccm)	d (nm)	σ (nm/min)
0.00	24.0	24
0.75	28.0	19
1.00	51.6	13
1.25	51.8	11
2.00	53.3	7

$f_{(Ar)} = 20$ sccm.

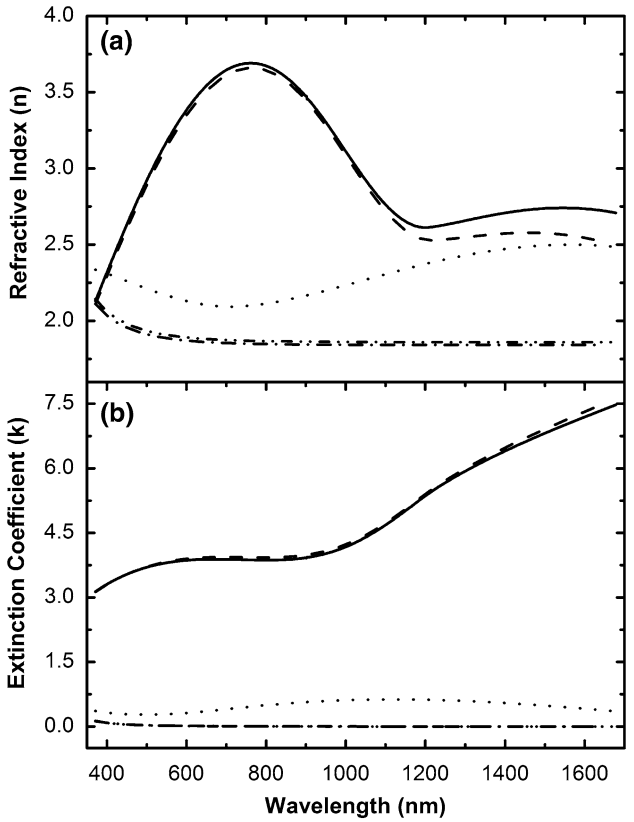

Fig. 6. Refractive index, n (a) and extinction coefficient, k (b) for MoO_x films deposited at oxygen flow rates of 0.00 sccm (solid line), 0.75 sccm (dashed line), 1 sccm (dotted line), 1.25 (dash-dot line) and 2.00 sccm (dash-dot-dot line).

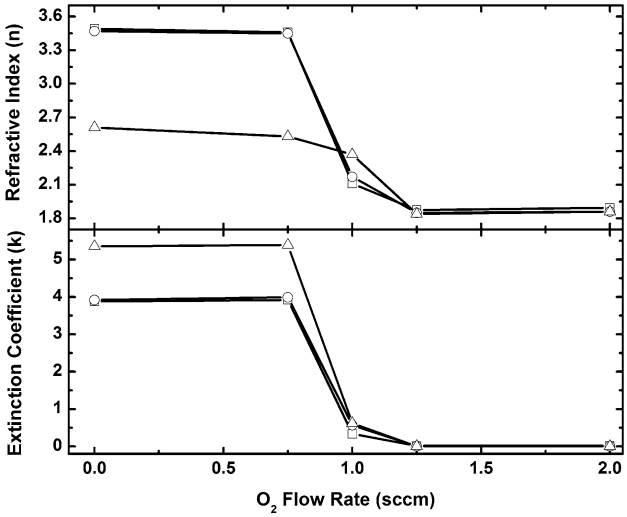

Fig. 7. Refractive index (n) and extinction coefficient (k) of molybdenum films versus oxygen flow rate for selected wavelengths: 632 (squares), 900 (circles), and 1200 nm (triangles). Lines are to guide the eye.

mentioned previously, show a clear effect on compound formation as a function of oxygen flow rate. Comparison of XPS data and optical measurements allows for the optical properties to be directly correlated to the compounds present within each film. At $f_{(O_2)}$ = 0.00 sccm and $f_{(Ar)}$ = 20.00 sccm, the films are metallic in nature, with trace amounts of surface oxide compounds, MoO_3, Mo_2O_5 and MoO_2. An increase in oxygen flow to a rate of 1.00 sccm represents the onset of oxide formation on the sputtering target surface resulting in a noticeable decrease in both refractive index and extinction coefficient for the grown films. The drop in both refractive index and extinction coefficient is the direct result of the formation of MoO_3 (Mo(VI)) as well as the reduced species Mo_2O_5 (Mo(V)). Formation of Mo_2O_5 can be associated with a marked increase in both n and k, as shown in Figs. 6 and 7. Based on the data shown in Fig. 5, it is evident that values of $f_{(O_2)}$ = 1.25 sccm or higher are necessary to form MoO_3 films without the presence of absorbing substoichiometric molybdenum-oxide compounds.

Transmission Measurements and Bandgap Calculation

Spectral transmission and reflectance measurements were collected in order to quantify the optical bandgap of films deposited with the different oxygen flow rates. To determine the bandgap, the absorption coefficient, α, was first determined using the measured spectral transmission and reflectivity. The bandgap (E_g) was calculated using the following relationship[1,27]:

$$\alpha h\nu = B(h\nu - E_g)^n \quad (1)$$

where the exponent, n, varies based on the band-to-band transitions accommodated by a given material,

Table III. Bandgaps for films deposited at varying flow rates

O_2 flow rate (sccm)	E_g (eV)
1.00	2.12
1.25	2.45
2.00	2.74

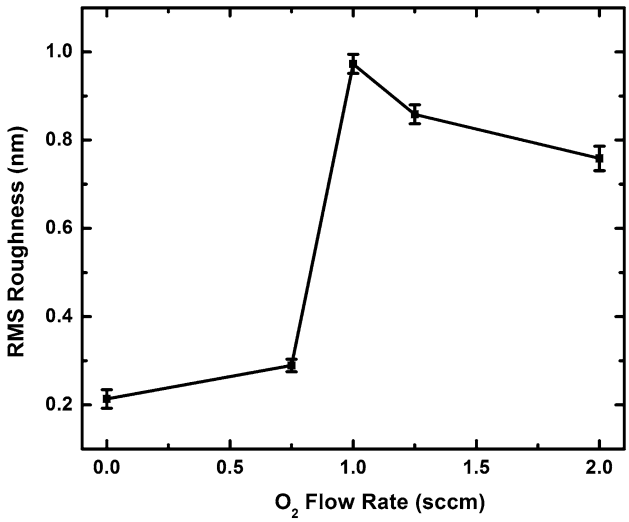

Fig. 8. Surface roughness as a function of oxygen flow rate as determined by AFM. Lines are to guide the eye.

B is a constant (set equal to 1 in this case) and $h\nu$ is the photon energy. For molybdenum oxides, the exponent is 2, due to their intrinsic ability to facilitate indirect-allowed band-to-band transitions.[68,73,74] A Tauc plot was then generated, wherein $(\alpha h\nu)^{1/2}$ ($eV^{1/2}$ $cm^{-1/2}$) was plotted as a function of photon energy, $h\nu$ (eV). The optical bandgap (E_g) was determined by extrapolating the linear portion of the plotted data to the corresponding photon energy where $(\alpha h\nu)^{1/2}$ is equal to zero.

The bandgaps listed in Table III indicate that E_g increases as a function of increasing oxygen flow. As shown in the high resolution XPS spectra (Fig. 5), the oxidation state associated with both depositions at $f_{(O_2)}$ = 1.25 sccm and 2.00 sccm is 6+, indicative of fully stoichiometric MoO_3. Differences in E_g can potentially be attributed to the reduction of defects associated with the formation of the fully stoichiometric compound. Furthermore, the lower bandgap associated with the film deposited at $f_{(O_2)}$ = 1.00 sccm was shown to contain substoichiometric Mo_2O_5 compounds associated with the presence of the 5+ valence state. The occurrence of the 5+ oxidation state was found via XPS analysis, as illustrated in Fig. 5. Absorption attributed to the 5+ oxidation state is likely the result of charge transfer between the molybdenum and oxygen species.[21,75] The presence of the further changes in bandgap is likely due

to the formation of oxygen inclusions within the film. The bandgap of 2.74, obtained for the MoO_3 film deposited at $f_{(O_2)}$ = 2.00 sccm, falls within the range of 2.67–2.76 as established by Miyata and Akiyoshi for amorphous MoO_3.[9,40]

Structural Characterization

Results of both atomic force microscopy (AFM) and XRR analyses indicate the presence of sub-nanometer roughness for all films deposited. Although roughness values are low, there is a discernible difference in surface morphology for different oxygen flow rates. This is illustrated in Fig. 8, in which the root mean squared roughness, as determined by AFM, increases with oxygen flow rate, from 0.2 nm at $f_{(O_2)}$ = 0.00 to a maximum value of 0.9 nm at $f_{(O_2)}$ = 1.00 sccm. The marked increase in surface roughness with the onset of target poisoning is likely a direct result of repeated interruption of local epitaxy induced by the formation of a surface oxide layer, leading to continuous renucleation within the growing film.[76,77] AFM composite images shown in Fig. 9 of three of the films provide visualization of this effect on surface morphology.

From the XRR data, the density of the films was determined from the total reflection or critical edge, film thickness was calculated from the period of the oscillations in the spectrum and surface roughness values were determined based on the rate of signal decay as a function of the detector angle (2θ). All calculations were performed using the Rigaku GlobalFit software package. Analysis of XRR data used a three-layer model consisting of silicon substrate, native silicon oxide layer, and the as-deposited film provided. Table IV contains the surface roughness, density and thickness as determined by XRR for all films. Since XRR interrogates a large lateral area compared with AFM, the roughness values are smaller. In addition to reflectivity measurements, GIXRD was performed on all samples. As illustrated in Fig. 10, GIXRD analysis

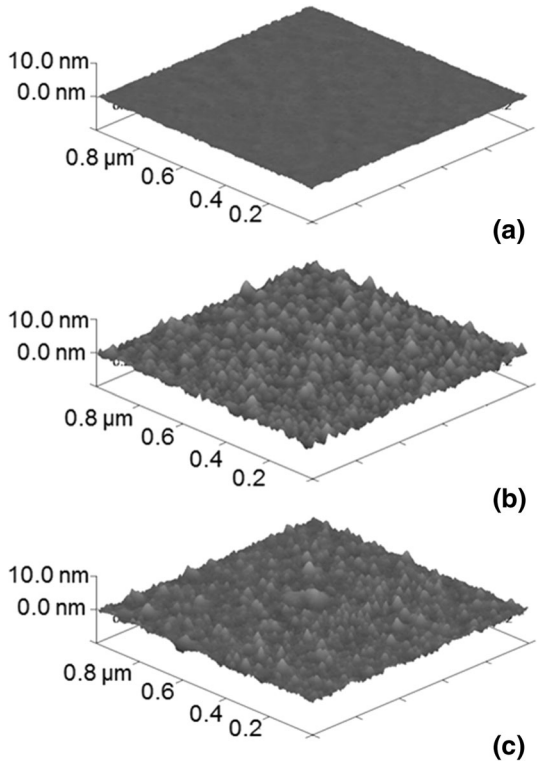

Fig. 9. AFM composite images showing surface roughness and morphology of films deposited at oxygen flow rates of 0.00 (a), 1.00 (b), and 2.00 sccm (c). Images are of a 1-μm^2 area.

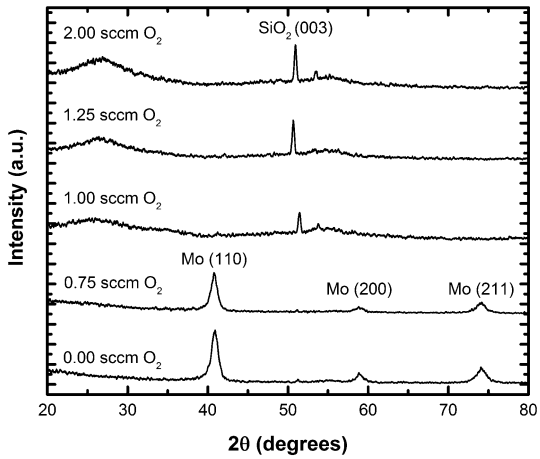

Fig. 10. Grazing incidence x-ray diffraction (GIXRD) spectra of MoO_x films deposited at varying oxygen flow rates. Peak assignments: body-centered cubic molybdenum: θ = 48.8° (110), θ = 58.9° (200) and θ = 74.1° (211); silicon dioxide: θ = 50.8° (003).

Table IV. List of parameters as determined by x-ray reflectivity analysis

O_2 flow rate (sccm)	Density (g/cm^3)	% of bulk density α-MoO_3	Surface roughness (nm)	Thickness (nm)
0.00	9.7	–	0.7	24.0
0.75	9.8	–	0.8	28.0
1.00	4.2	89.0	0.6	51.6
1.25	3.8	80.6	0.8	51.8
2.00	3.8	80.6	0.9	53.3

The bulk density of α-MoO_3 is 4.71 g/cm^3.[67]

was able to show that the degree of crystallinity present within the films varied dramatically as a function of oxygen content. Films deposited at flow rates of 0.00 sccm and 0.75 sccm O_2 demonstrated significant crystalline character, with peaks characteristic of body-centered cubic molybdenum located at $\theta = 48.8°$ (110), $\theta = 58.9°$ (200) and $\theta = 74.1°$ (211). At higher oxygen flow rates coinciding with the onset of formation of molybdenum oxides, the films are shown to be amorphous. Sharp crystalline peaks around $\theta = 50.8°$ present within those spectra are the result of x-ray interaction with the native oxide layer on the (100) silicon substrate.[48]

CONCLUSIONS

Deposition using MPPMS within the poisoned regime ($f_{(O_2)} \geq 1.25$ sccm) allowed for the fabrication of amorphous, transparent MoO_3 with bandgaps of 2.45 and 2.74 eV at flow rates of 1.25 sccm and 2.00 sccm O_2, respectively. SE studies of these films indicated negligible values for the extinction coefficient (k) at energies below 2.45 eV. Fully stoichiometric MoO_3 films, as verified by XPS analysis, were only obtained from sputter depositions where the target surface was fully poisoned. Films deposited at flow rates of 0.00 sccm and 0.75 sccm O_2 were shown to have higher densities, corresponding to elemental molybdenum (10.18 g/cm^3)[9] and crystalline structure associated with body center cubic Mo. Correspondingly, these films were the only specimens that possessed 3d transitions associated with Mo^0 ($3d_{5/2}$ = 226.9 eV). Films deposited within the transition region, at 1.00 sccm O_2, consisted largely of mixed Mo^{6+} and Mo^{5+} oxidation states, corresponding to MoO_3 and Mo_2O_5 compounds. The presence of the Mo_2O_5 compound is associated with increased absorption and a net reduction of the optical bandgap to 2.12 eV. AFM and XRR analysis concluded that the surface roughness values were below 1 nm for all films, with roughness values increasing alongside oxygen partial pressure until reaching a maximum value at 1.00 sccm O_2. Based on measurements of density, absorption, and chemical state, it can be concluded that films deposited at oxygen flow rates at and below $f_{(O_2)} = 0.75$ sccm are metallic in nature, while films deposited at and above $f_{(O_2)} = 1.00$ sccm were shown to be insulating. The identification of the metal–dielectric transition provides a useful process–property relationship for increased understanding of the MPPMS deposition conditions needed to fabricate highly dense, transparent MoO3 thin films with average surface roughness values below 1 nm.

REFERENCES

1. R. Sundararaman and C. Song, *Ind. Eng. Chem. Res.* 53, 1890 (2014).
2. J.G. Choi and L. Thompson, *Appl. Surf. Sci.* 93, 143 (1996).
3. I.E. Wachs, *Catal. Today* 27, 437 (1996).
4. D.S. Kim, I.E. Wachs, and K. Segawa, *J. Catal.* 149, 268 (1994).
5. T. He and J. Yao, *J. Photochem. Photobiol. C* 4, 125 (2003).
6. S. Kubota, K. Kanomata, K. Momiyama, T. Suzuki, and F. Hirose, *IEICE Trans. Electron.* 96, 604 (2013).
7. M. Zhang, Z. Chen, L. Xiao, B. Qu, and Q. Gong, *J. Appl. Phys.* 113, 113105 (2013).
8. G. Nazri and G. Pistoia, *Lithium Batteries: Science and Technology* (New York: Springer, 2003), p. 92.
9. S. Mohamed, O. Kappertz, J. Ngaruiya, T.L. Pedersen, R. Drese, and M. Wuttig, *Thin Solid Films* 429, 135 (2003).
10. J. Besenhard, J. Heydecke, and H. Fritz, *Solid State Ion.* 6, 215 (1982).
11. J. Besenhard, J. Heydecke, E. Wudy, H. Fritz, and W. Foag, *Solid State Ion.* 8, 61 (1983).
12. X. Haitao and Z. Xiang, *J. Appl. Phys.* 114, 244505 (2013).
13. P. Qin, G. Fang, W. Ke, F. Cheng, Q. Zheng, J. Wan, H. Lei, and X. Zhao, *J. Mater. Chem. A* 110, 63 (2014).
14. Y. Sun, J. Wang, B. Zhao, R. Cai, R. Ran, and Z. Shao, *J. Mater. Chem. A* 1, 4736 (2013).
15. H. Simchi, B.E. McCandless, T. Meng, and W.N. Shafarman, *J. Appl. Phys.* 115, 033514 (2014).
16. M. Ferroni, V. Guidi, G. Martinelli, P. Nelli, M. Sacerdoti, and G. Sberveglieri, *Thin Solid Films* 307, 148 (1997).
17. E. Comini, L. Yubao, Y. Brando, and G. Sberveglieri, *Chem. Phys. Lett.* 407, 368 (2005).
18. D. Mutschall, K. Holzner, and E. Obermeier, *Sens. Actuators B* 36, 320 (1996).
19. W. Moshier, G. Davis, and G. Cote, *J. Electrochem. Soc.* 136, 356 (1989).
20. V. Nirupama, K. Gunasekhar, B. Sreedhar, and S. Uthanna, *Curr. Appl. Phys.* 10, 272 (2010).
21. T.S. Sian and G. Reddy, *Sol. Energy Mater. Sol. Cells* 82, 375 (2004).
22. M. Al-Kuhaili, S. Durrani, I. Bakhtiari, and A. Al-Shukri, *Opt. Commun.* 283, 2857 (2010).
23. F. Werfel and E. Minni, *J. Phys. C* 16, 6091 (2000).
24. D.O. Scanlon, G.W. Watson, D. Payne, G. Atkinson, R. Egdell, and D. Law, *J. Phys. Chem. C* 114, 4636 (2010).
25. O. Marin-Flores, L. Scudiero, and S. Ha, *Surf. Sci.* 603, 2327 (2009).
26. J. Horkans and M. Shafer, *J. Electrochem. Soc.* 124, 1202 (1977).
27. Y. Shi, B. Guo, S.A. Corr, Q. Shi, Y. Hu, K.R. Heier, L. Chen, R. Seshadri, and G.D. Stucky, *Nano Lett.* 9, 4215 (2009).
28. Y. Sun, X. Hu, C.Y. Jimmy, Q. Li, W. Luo, L. Yuan, W. Zhang, and Y. Huang, *Energy Environ. Sci.* 4, 2870 (2011).
29. Y. Sun, X. Hu, W. Luo, and Y. Huang, *ACS Nano* 5, 7100 (2011).
30. Y. Xu, R. Yi, B. Yuan, X. Wu, M. Dunwell, Q. Lin, L. Fei, S. Deng, P. Andersen, and D. Wang, *J. Phys. Chem. Lett.* 3, 309 (2012).
31. H. Zhang, K. Wang, X. Wu, Y. Jiang, Y. Zhai, C. Wang, X. Wei, and J. Chen, *Adv. Funct. Mater.* 11, 1328 (2014).
32. H. Martínez, J. Torres, M. Rodríguez-García, and L.L. Carreño, *Physica B* 407, 3199 (2012).
33. H. Martínez, J. Torres, L. López-Carreño, and M. Rodríguez-García, *J. Supercond. Nov. Magn.* 26, 2485 (2013).
34. A. Bouzidi, N. Benramdane, H. Tabet-Derraz, C. Mathieu, B. Khelifa, and R. Desfeux, *Mater. Sci. Eng. B* 97, 5 (2003).
35. S. Chuang, C. Battaglia, A. Azcatl, S. McDonnell, J.S. Kang, X. Yin, M. Tosun, R. Kapadia, H. Fang, and R.M. Wallace, *Nano Lett.* 14, 1337 (2014).
36. C. Battaglia, X. Yin, M. Zheng, I.D. Sharp, T.L. Chen, A. Azcatl, S. McDonell, C. Carraro, R. Maboudian, and R.M. Wallace, *Nano Lett.* 14, 967 (2014).
37. C. Ramana, V. Atuchin, L. Pokrovsky, U. Becker, and C. Julien, *J. Vac. Sci. Technol. A* 25, 1166 (2007).
38. C. Ramana and C. Julien, *Chem. Phys. Lett.* 428, 114 (2006).
39. S. Sunu, E. Prabhu, V. Jayaraman, K. Gnanasekar, and T. Gnanasekaran, *Sens. Actuators B* 94, 189 (2003).
40. N. Miyata and S. Akiyoshi, *J. Appl. Phys.* 58, 1651 (1985).
41. M. Rouhani, Y.L. Foo, J. Hobley, J. Pan, G.S. Subramanian, X. Yu, A. Rusydi, and S. Gorelik, *Appl. Surf. Sci.* 273, 150 (2013).

42. J.-. Faou, E. Barthel, and S.Y. Grachev, *Thin Solid Films* 527, 222 (2013).
43. V. Nirupama and S. Uthanna, *J. Mater. Sci.* 21, 45 (2010).
44. J. Lin, W.D. Sproul, J.J. Moore, S. Lee, and S. Myers, *Surf. Coat. Technol.* 205, 3226 (2011).
45. L. Meng, T. Cho, S. Jung, and D. Ruzic, *IEEE ICOPS* 1, 1 (2011).
46. M. Hála, J. Čapek, O. Zabeida, J. Klemberg-Sapieha, and L. Martinu, *J. Phys. D* 45, 055204 (2012).
47. J. Lin, W.D. Sproul, J.J. Moore, Z. Wu, S. Lee, R. Chistyakov, and B. Abraham, *JOM* 63, 48 (2011).
48. J. Lin, J.J. Moore, W.D. Sproul, S.L. Lee, and J. Wang, *IEEE Trans. Plasma Sci.* 38, 3071 (2010).
49. J. Lin, J. Moore, W. Sproul, B. Mishra, J. Rees, Z. Wu, R. Chistyakov, and B. Abraham, *Surf. Coat. Technol.* 203, 3676 (2009).
50. B. Liebig, N.S.J. Braithwaite, P. Kelly, R. Chistyakov, B. Abraham, and J. Bradley, *Surf. Coat. Technol.* 205, S312 (2011).
51. K. Sarakinos, J. Alami, and M. Wuttig, *J. Phys. D* 40, 2108 (2007).
52. S. Konstantinidis, J. Dauchot, and M. Hecq, *Thin Solid Films* 515, 1182 (2006).
53. D. Depla, S. Heirwegh, S. Mahieu, J. Haemers, and R. De Gryse, *J. Appl. Phys.* 101, 013301 (2007).
54. V. Kouznetsov, K. Macák, J.M. Schneider, U. Helmersson, and I. Petrov, *Surf. Coat. Technol.* 122, 290 (1999).
55. S. Dushman, *Rev. Sci. Instrum.* 20, 139 (1949).
56. A. Phelps and Z.L. Petrovic, *Plasma Sources Sci. Technol.* 8, R21 (1999).
57. T. Lange, W. Njoroge, H. Weis, M. Beckers, and M. Wuttig, *Thin Solid Films* 365, 82 (2000).
58. D. Depla and R. De Gryse, *Surf. Coat. Technol.* 183, 184 (2004).
59. J. Alami, P. Persson, D. Music, J. Gudmundsson, J. Bohlmark, and U. Helmersson, *J. Vac. Sci. Technol. A* 23, 278 (2005).
60. D. Depla and R. De Gryse, *Surf. Coat. Technol.* 183, 190 (2004).
61. W.D. Sproul, J. Lin, and J.J. Moore, *SVC Spring Bulletin* 28, 1 (2009).
62. S. Berg and T. Nyberg, *Thin Solid Films* 476, 215 (2005).
63. W.D. Sproul, D.J. Christie, and D.C. Carter, *Thin Solid Films* 491, 1 (2005).
64. B. Mishra, J. Moore, J.L. Lin, and W. Sproul, *Trans. Tech. Publ.* 638, 208 (2010).
65. N. Fairley, Casa Software Ltd CasaXPS 2.3.16 (1999–2011).
66. J. Lin, J.J. Moore, W.D. Sproul, B. Mishra, Z. Wu, and J. Wang, *Surf. Coat. Technol.* 204, 2230 (2010).
67. D. Guttler, B. Abendroth, R. Grotzschel, W. Moller, and D. Depla, *Appl. Phys. Lett.* 85, 6134 (2004).
68. V. Nirupama, M.C. Sekhar, T. Subramanyam, and S. Uthanna, *J. Phys.* 208, 012101 (2010).
69. J.F. Moulder, J. Chastain, and R.C. King, *Handbook of X-ray Photoelectron Spectroscopy: A Reference Book of Standard Spectra for Identification and Interpretation of XPS Data* (Eden Prairie, MN: Physical Electronics, 1995), p. 65.
70. C.R. Clayton and Y.C. Lu, *Surf. Interface Anal.* 14, 66 (1989).
71. C.V. Ramana, V.V. Atuchin, V. Kesler, V. Kochubey, L. Pokrovsky, V. Shutthanandan, U. Becker, and R.C. Ewing, *Appl. Surf. Sci.* 253, 5368 (2007).
72. Y.C. Liu, J.H. Hsieh, and S.K. Tung, *Thin Solid Films* 510, 32 (2006).
73. J.I. Pankove, *Absorption* (New York: Dover Publications, 1971), p. 34.
74. C.G. Granqvist, *Handbook of Inorganic Electrochromic Materials* (New York: Elsevier Science, 1995), p. 217.
75. B.W. Faughnan and R.S. Crandall, *Appl. Phys. Lett.* 31, 834 (1977).
76. M.A.P.B. Barna, *Thin Solid Films* 317, 27 (1998).
77. I. Petrov, P. Barna, L. Hultman, and J. Greene, *J. Vac. Sci. Technol. A* 21, S117 (2003).